On Nonlinear Doubly-Diffusive Marangoni Instability

Enhancement of simultaneous heat and mass transfer due to surface tension gradient-induced Marangoni convection is studied. The geometry considered is a thin liquid film between a solid phase and a gas phase. In regions where the two Marangoni numbers are of opposite signs (quadrants II and IV), Orr-Sommerfeld analysis reveals the possibility of oscillatory roll cells. A nonlinear bifurcation study of the amplitude equations indicates that the finite-amplitude oscillatory rolls are annihilated by steady rolls slightly beyond the oscillatory stability boundary in a heteroclinic bifurcation. Oscillatory rolls are hence restricted to quadrants II and IV. Finite-amplitude instability due to subcritical bifurcation of the steady rolls is also shown to be limited to these quadrants. In addition to classifying the bifurcations, the numerical study also provides a useful correlation for single-component flux enhancement, $Nh^* = 1 + 0.001324\, Nu^{0.23} Pr^{0.16} (N_T - N_T^c)$, which is compared to available experimental data.

Kwok-Lun Ho, Hsueh-Chia Chang
Department of Chemical Engineering
University of Notre Dame
Notre Dame, IN 46556

Introduction

Heat and mass transfer between a solid and a gas phase through a liquid film with a gas/liquid free surface is an important phenomenon in many chemical processes. In this work we address the simplest case in which there is no bulk flow in the liqiud phase. (Flow in the gas phase is permissible since heat and mass transport on the gas side is described by effective transfer coefficients.) This is not to say that the liquid is everywhere stationary since, for sufficiently large driving forces, convective roll cells may appear below the interface and greatly enhance the net heat and mass flux across the liquid film, normally by severalfold. The mechanism behind these convective roll cells can be buoyancy (the Rayleigh-Benard instability). Alternatively, surface tension at the interface can vary due to temperature and/or concentration gradients. This surface tension gradient will, in turn, cause fluid flow in the liquid phase. In thin-film processes in chemical microelectronic industries, heat and mass enhancement is mostly due to this Marangoni effect. Certainly, in cases with only mass transfer, Rayleigh-Benard instability should make a negligible contribution since density is a weak function of concentration. Another industry where Marangoni instability is of paramount importance is, of course, any outer-space technology involving free surfaces. Earlier Apollo experiments (Grodzka and Bannister, 1972) have positively confirmed the serious limitations imposed by Marangoni instability. We shall study the Marangoni phenomenon under two independent driving forces, the doubly-diffusive Marangoni instability. They can correspond to a temperature gradient and a concentration gradient or to two independent concentration gradients. We shall predict the onset of the Marangoni effect and qualitative behavior of the convective roll cells (viz., stationary, oscillatory, supercritical, or subcritical bifurcations) with a linear Orr-Sommerfeld type stability analysis and a normal form bifurcation analysis about a particular singularity. In addition, we shall quantitatively predict, within the limitation of our assumptions, the degree of flux enhancement due to the Marangoni phenomenon. This will be a nonlinear analysis that includes a major numerical effort to overcome the free surface problem. However, it also contains a bifurcation analysis near critical system conditions for instability. The bifurcation results, although only locally valid, have the advantages of yielding a simple correlation-type expression for heat and mass transfer enhancements and of clarifying the occurrence of subcritical finite-amplitude instability and competition between steady and oscillatory modes.

Early work on the single-gradient Marangoni instability by Pearson (1958) and Sternling and Scriven (1959, 1963) focused on the prediction of onset of static instability by an Orr-Som-

Correspondence concerning this paper should be addressed to Hsueh-Chia Chang.
The present address of Kwok-Lun Ho is Department of Chemical Engineering, University of Minnesota, Minneapolis, MN 55455.

merfeld analysis. That the principle of exchange of stability is valid was proven by Vidal and Acrivos (1966). It was not until 1983 that the doubly-diffusive Marangoni instability due to consecutive heat and mass transfer was analyzed, by McTaggart (1983). She computed the characteristic equation that governed the static stability boundary (with zero leading eigenvalue) and located the boundary in the parameter space. In addition, she also showed the existence of oscillatory instability (Hopf bifurcation) for simplified boundary conditions, namely zero heat and mass transfer coefficients at the interface. Exchange of stability is hence not valid for the doubly-diffusive Marangoni problem. While McTaggart was able to demonstrate the existence of the oscillatory stability boundaries, she was unable to unify them with the static boundaries in a systematic manner to produce the true stability boundaries in the parameter space. We shall complete the linear stability analysis done by McTaggart. All the stability boundaries in the parameter space will be rigorously derived. Furthermore, we shall demonstrate that oscillatory instability is only possible if the Marangoni numbers for heat (N_T) and mass (N_C) transfer are of opposite signs, that is, when the two fluxes are in opposite directions or when the two components have opposite effects on the surface tension.

Although a great deal of progress has recently been made on the nonlinear analysis of the Benard problem (Tavantzis et al., 1978; Nagata and Thomas, 1986; Knobloch et al., 1986), the nonlinear Marangoni problem (singly or doubly diffusive) has not been attempted in any of the previous work cited above. The main difficulties are the interfacial boundary conditions. The mass balance condition is a mixed type boundary condition since heat transfer coefficients are used on the gas side. The tangential stress balance must account for the net pull due to surface tension gradient and is also quite complex. These difficult conditions do not exist for the simpler Benard problem. As a result, even for the linear Orr-Sommerfeld analysis by McTaggart and in this paper, the eigenfunctions that satisfy all the boundary conditions are extremely complicated. This rules out the perturbation approach taken by Tavantzis et al. (1978) for the nonlinear Benard problem since the necessary manipulations and inner products would be far too difficult to manage even with a symbolic machine.

We overcome the difficulty of the free-surface boundary conditions by formulating a unique spectral numerical method for the nonlinear problem. Orthogonal basis functions that satifsy all boundary conditions except the problematic free-surface conditions are constructed from Jacobi polynomials. The dependent variables are then expanded by these basis functions and inner products are taken with the same basis set, as in other spectral methods, with proper weighting to expedite convergence. However, the number of basis functions used in the expansion is purposely chosen to exceed the number of inner products such that the number of projected ordinary differential equations (ODE's) is smaller than the total number of expansion coefficients. The additional degrees of freedom are used to satisfy the unaccounted for free-surface conditions. One is hence left with a set of ODE's that is coupled to a complementary set of algebraic equations. Insofar as the free-surface conditions are linear, the algebraic equations are also linear and one can easily invert them to solve for the additional coefficients. Upon substitution into the ODE's, an independent set of ODE's results, as in the conventional spectral method. We verify the validity of this tau-spectral method first mentioned in Gottlieb and Orszag (1977) by demonstrating exponential convergence with respect to mode number.

A bifurcation analysis is then applied to the set of first-order ODE's. The dynamic portraits near the stability boundaries are classified using center manifold projection and normal form techniques. Subcritical finite-amplitude instability and mode competition are all clearly described. Quantitative estimates for the enhancement factor of heat and mass transfer (overall Nusselt number) are also available from the bifurcation analysis. These are favorably compared to the numerical values from the full 80-mode expansion and to experimental data measured by Palmer and Berg (1971).

Mathematical Formulations

The doubly-diffusive problem of heat and mass transfer between a solid and a gas through a thin liquid film B with infinite horizontal length depicted in Figure 1 is studied. A is an inviscid gas phase. Except for surface tension, all physical properties of the liquid film and the gas phase are assumed to be constant. In addition, we assume that the temperature and solutal concentration at the bottom of the film are constant. At the top of the film, heat and mass fluxes from the film interface to the gas phase, which may involve mathematically intractable, highly turbulent transport equations, are described by heat and mass transfer coefficients with appropriately defined gas phase Nusselt numbers. For the present case, the thickness L of the film is assumed to be small enough so that body forces on the film can be neglected. Alternatively, one would be concerned with processes in a microgravity environment.

With the above assumptions, we can write the Navier-Stokes equation, the continuity equation for imcompressible flow, and the heat and mass transfer equations as follows:

$$\frac{\partial U}{\partial t} + U \cdot \nabla U = \frac{-1}{\rho} \nabla p + \nu \nabla^2 U \tag{1a}$$

$$\nabla \cdot U = 0 \tag{1b}$$

$$\frac{\partial T}{\partial t} + U \cdot \nabla T = \kappa \nabla^2 T \tag{1c}$$

$$\frac{\partial C}{\partial t} + U \cdot \nabla C = D \nabla^2 C \tag{1d}$$

for a thin film with infinite length. U is the two-dimensional

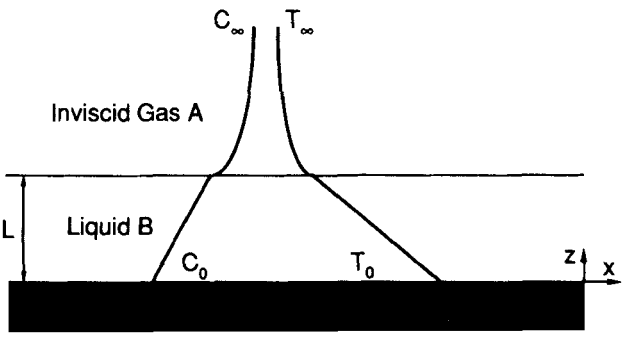

Figure 1. System studied.
Temperature and conversion profiles correspond to the purely conductive and diffusive base state

velocity field with components (u, w); κ and D are the thermal diffusivity of the film and diffusivity of the species, respectively; C is the solutal concentration of the diffusing species; T can be considered as a temperature or a second concentration quantity. In the latter case, κ will also be a diffusivity.

A solution exists under all conditions for Eqs. 1, with the appropriate boundary conditions to be defined later, Eqs. 8. This corresponds to the purely conductive and diffusive base state with no convection:

$$U = 0 \tag{2a}$$

$$T = T_b = T_0 + \frac{z\Delta T_0}{L} \tag{2b}$$

$$C = C_b = C_0 + \frac{z\Delta C_0}{L} \tag{2c}$$

where T_0 and C_0 are the temperature and solutal concentration, respectively, at $z = 0$, and ΔT_0 and ΔC_0 are the differences across the film (top-bottom) of the two quantities. With heat and mass balances at the base state, one can find the expressions of ΔT_0 and ΔC_0 in terms of T_0, T_∞, C_0, and C_∞:

$$\Delta T_0 = \frac{Nu(T_\infty - T_0)}{Nu + 1} \tag{3a}$$

and

$$\Delta C_0 = \frac{Sh(C_\infty - C_0)}{Sh + 1} \tag{3b}$$

where Nu and Sh are the Nusselt and Sherwood numbers for the gas phase,

$$Nu = \frac{h_T L}{\rho c_p \kappa} \qquad Sh = \frac{h_m L}{\rho D}$$

where h_T and h_m are the heat and mass transfer coefficients. However, this solution is not always stable and we shall seek parameter values for which it is stable. The boundaries in the parameter space that demarcate the stable region from the unstable region are known as the stability boundaries. Note that at the base state, the heat flux and the mass flux are $-k\Delta T_0/L$ and $-D\Delta C_0/L$, respectively, where k is the thermal conductivity.

We first assume that the system is two-dimensional so that we can represent the fluid motion by a stream function ψ:

$$\frac{\partial \psi}{\partial t} + J(\psi, \nabla^2\psi) = \nu\nabla^4\psi \tag{4}$$

where $u = -\psi_z$ and $w = \psi_x$. Note that the base state for the stream function ψ_b is zero, and thus Eq. 4 has the same form as its deviation form. By restricting ourselves to two-dimensional systems, only convective rolls can be studied here. Hexagonal and square cells must be ruled out. In this connection, it should be mentioned that for the Benard problem Schlüter et al. (1965) have verified that the rolls are superior to hexagons and squares in flux enhancement and have been assumed to be the preferred planforms of the fluids.

We use the following deviation variables, which measure the departure of T and C from their base states,

$$S = T - T_b \tag{5a}$$

$$G = C - C_b \tag{5b}$$

and rewrite Eqs. 1c and 1d by using the definitions of T_b and C_b:

$$\frac{\partial S}{\partial t} + J(\psi, S) = -\psi_x\theta + \kappa\nabla^2 S \tag{6a}$$

$$\frac{\partial G}{\partial t} + J(\psi, G) = -\psi_x\phi + D\nabla^2 G \tag{6b}$$

where $J(f, g) = f_x g_z - f_z g_x$, and θ and ϕ are the base state temperature and solutal concentration gradients, respectively: $\theta = \Delta T_0/L$, $\phi = \Delta C_0/L$.

To write the system of equations in dimensionless form we introduce scaling quantities $x \to xL$, $z \to zL$, $\psi \to \psi\nu$, $\nabla \to \nabla/L$, $S \to S\theta L$, $G \to G\phi L$, and $t \to tL^2/\nu$. After some manipulations, the system becomes:

$$\frac{\partial \psi}{\partial t} + J(\psi, \nabla^2\psi) = \nabla^4\psi \tag{7a}$$

$$\frac{\partial S}{\partial t} + J(\psi, S) = Pr^{-1}\nabla^2 S - \frac{\partial \psi}{\partial x} \tag{7b}$$

$$\frac{\partial G}{\partial t} + J(\psi, G) = Pr^{-1}e^{-1}\nabla^2 G - \frac{\partial \psi}{\partial x} \tag{7c}$$

Here $Pr = \nu/\kappa$ is the Prandtl number, and $e = \kappa/D$ is the Lewis number.

In the vertical direction, we use the boundary conditions

$$\psi = \psi_z = S = G = 0, \quad \text{at } z = 0 \tag{8a–8d}$$

These are no-slip conditions for the fluid and constant temperature and solutal concentration at the bottom of the film, as stated above. We assume a rigid planar free surface with the following boundary condition:

$$\psi = 0, \quad \text{at } z = 1 \tag{8e}$$

This corresponds to the high surface tension case with negligible deflection and normal stress, that is, vanishing "crispation number." The fact that heat (mass) flux across the interface is proportional to a heat (mass) transfer coefficient directly implies the boundary conditions:

$$S_z + NuS = G_z + ShG = 0, \quad \text{at } z = 1 \tag{8f, 8g}$$

where Nu and Sh are the previously defined gas-side Nusselt and Sherwood numbers for heat and mass transfer from the free surface to the gas phase, respectively. Note that since the pertinent instability mechanism is due to surface tension variation on

the free surface, Dirichlet boundary conditions $S = G = 0$ (corresponding to $Nu = Sh = \infty$) that are often applied to Benard problems cannot be used here. This is one complexity of the Marangoni problem that prevents easy solution. The other key boundary condition at $z = 1$ is the tangential stress balance:

$$\psi_{zz} + Pr^{-1}e^{-1}N_C G_x + Pr^{-1}N_T S_x = 0 \quad \text{at } z = 1 \qquad (8h)$$

where N_T and N_C are the heat and mass transfer Marangoni numbers, respectively:

$$N_T = \frac{\sigma_T \theta L^2}{\kappa\mu} = \frac{\sigma_T \Delta T_0 L}{\kappa\mu} \qquad N_C = \frac{\sigma_c \phi L^2}{D\mu} = \frac{\sigma_c \Delta C_0 L}{D\mu}$$

and the surface tension is assumed to be a linear function of C and T with gradients σ_c and σ_T. Note that depending on the effects of C and T (which, again, could be two species concentrations) on the surface tension and depending on the direction of the two driving forces, N_T and N_C can take on both positive and negative values.

We shall assume in the nonlinear problem that the convective rolls are spatially periodic with wavelength a, which is determined by the fastest growing wave number from the Orr-Sommerfeld analysis. Hence, the appropriate boundary conditions in the horizontal directions are

$$S_x = G_x = \psi = \psi_{xx} = 0 \quad \text{at } x = 0 \quad \text{and } a/2 \qquad (9a\text{–}9d)$$

These conditions correspond to zero heat and mass fluxes, and no tangential viscous stresses on the side and the middle of the cell. Note that we have used the symmetry of two convective rolls in a cell. The above boundary conditions at $x = 0$ are also symmetric with respect to reflection. Hence, the problem is confined to half a unit cell in a periodic sequence of roll cells.

Orr-Sommerfeld Analysis

Assuming disturbances of arbitrary horizontal wave number α, the solution for the linear system is written as

$$\psi = e^{\beta t}e^{i\alpha x}P(z) \qquad (10a)$$

$$S = e^{\beta t}e^{i\alpha x}H(z) \qquad (10b)$$

$$G = e^{\beta t}e^{i\alpha x}Q(z) \qquad (10c)$$

These dimensionless equations are substituted into the linearized version of Eq. 7 (which simply omits all J terms) to give the following equations:

$$(D^2 - \alpha^2)(D^2 - \alpha^2 r^2)P(z) = 0 \qquad (11)$$

$$(D^2 - \alpha^2 q^2)H(z) = iPr\alpha P(z) \qquad (12)$$

$$(D^2 - \alpha^2 f^2)Q(z) = iPre\alpha P(z) \qquad (13)$$

where $r^2 = 1 + \lambda$

$g^2 = 1 + Pr\lambda$

$f^2 = 1 + Pre\lambda$

and $\lambda = \beta/\alpha^2$

Whereas the boundary conditions become:

$$P = P_z = H = Q = 0 \quad \text{at } z = 0$$

and $$P = H_z + NuH = Q_z + ShQ$$
$$= (D^2 + \alpha^2)P + i\alpha Pr^{-1}e^{-1}N_C Q$$
$$+ i\alpha Pr^{-1}N_T H = 0 \quad \text{at } z = 1$$

which is easier to manipulate. Expanding the eigenfunctions P, H, and Q in the following series of hyperbolic sines and cosines,

$$P(z) = A_1 \sinh(\alpha z) + A_2 \cosh(\alpha z) + A_3 \sinh(\alpha r z) + A_4 \cosh(\alpha r z)$$

$$H(z) = B_1 \sinh(\alpha z) + B_2 \cosh(\alpha z) + B_3 \sinh(\alpha r z) + B_4 \cosh(\alpha r z) + B_5 \sinh(\alpha g z) + B_6 \cosh(\alpha g z)$$

$$Q(z) = C_1 \sinh(\alpha z) + C_2 \cosh(\alpha z) + C_3 \sinh(\alpha r z) + C_4 \cosh(\alpha r z) + C_5 \sinh(\alpha f z) + C_6 \cosh(\alpha f z)$$

and inserting into Eqs. 11 to 13 and the boundary conditions, we obtain with the aid of a symbolic machine (MACSYMA), the characteristic equation,

$$\frac{N_c(ePrS_f X_1 + fC_f X_2 + fX_3 + S_f X_4)}{ePr(ePr - 1)(S_f Sh + \alpha f C_f)\lambda^3} + \frac{N_T(PrS_g X_1 + qC_g X_2 + gX_3 + S_g X_4)}{Pr(Pr - 1)(S_g Nu + \alpha g C_g)\lambda^3} + \frac{\alpha X_2}{\lambda} = \frac{\Sigma}{\lambda^3} = \phi = 0 \qquad (14)$$

where

$$X_1 = r^2 SS_r + SS_r + 2r - 2rCC_r$$
$$X_2 = CS_r - rSC_r$$
$$X_3 = rS - S_r$$
$$X_4 = rCC_r - SS_r - r$$

and $S = \sinh(\alpha)$, $C = \cosh(\alpha)$, $S_a = \sinh(\alpha a)$, $C_a = \cosh(\alpha a)$. Unlike McTaggart (1983), who was only able to obtain analytical equations for the simple bifurcation curves, we have developed the complete characteristic equation for the problem. For details of the symbolic manipulation, see the thesis of Ho (1987).

Simple bifurcation corresponds to a zero growth rate of the disturbance with no temporal oscillation. The bifurcation curve can be obtained at the limit of $\lambda \to 0$ in Eq. 14. However, it is found that the term Σ in the equation has a zero root multiplicity three. In fact, the reason for writing Σ/λ^3 is to remove this singularity when λ is approaching zero. Hence we expand Σ in a Taylor series, divide the series by λ^3, and take the limit $\lambda \to 0$ (Ho, 1987). The simple bifurcation curve, which is a straight line in the Marangoni plane, is given by:

$$\frac{N_T}{Nu \sinh(\alpha) + \alpha \cosh(\alpha)} + \frac{N_C}{Sh \sinh(\alpha) + \alpha \cosh(\alpha)} - \frac{8\alpha[\cosh(\alpha)\sinh(\alpha) - \alpha]}{\sinh^3(\alpha) - \alpha^3 \cosh(\alpha)} = F = 0 \qquad (15)$$

Table 1. Critical N_T for a Single Driving Force

Nu	N_T^c	α_c	Nu	N_T^c	α_c
0.019379	80.35143	2.00	3.278205	193.6719	2.50
0.076053	82.51697	2.02	3.570916	203.4099	2.52
0.1359021	84.78517	2.04	3.890490	214.0087	2.54
0.1991348	87.16265	2.06	4.240493	225.5826	2.56
0.2659776	89.65662	2.08	4.625147	238.2670	2.58
0.3366768	92.27492	2.10	5.049492	252.2236	2.60
0.4115005	95.02608	2.12	6.042798	284.7720	2.64
0.4907416	97.91942	2.14	6.042798	284.7720	2.64
0.5747199	100.9652	2.16	6.628137	303.8890	2.66
0.6637863	104.1745	2.18	7.286788	325.3562	2.68
0.7583258	107.5596	2.20	8.032778	349.6234	2.70
0.8587623	111.1342	2.22	8.883952	377.2629	2.72
0.9655635	114.9131	2.24	9.863361	409.0139	2.74
1.079246	118.9129	2.26	11.00132	445.8486	2.76
1.200384	123.1519	2.28	12.33848	489.0713	2.78
1.329615	127.6504	2.30	13.93073	540.4735	2.80
1.467650	132.4313	2.32	15.85695	602.5856	2.82
1.615284	137.5199	2.34	18.23228	679.1005	2.84
1.773411	142.9449	2.36	21.23166	775.6287	2.86
1.943034	148.7384	2.38	25.13437	901.1277	2.88
2.125290	154.9368	2.40	30.41555	1070.837	2.90
2.321469	161.5813	2.42	37.95433	1312.951	2.92
2533.039	168.7191	2.44	49.57911	1686.115	2.94
2.761680	176.4039	2.46	69.82263	2335.705	2.96
3.009324	184.6976	2.48	113.8555	3748.287	2.98

This result is in exact agreement with that obtained by Sternling and Scriven (1963) and McTaggart (1983). In fact, for the single-component case ($N_C = 0$), Eq. 15 yields the classical result of Pearson (1958). The critical Marangoni number N_T^c is 80 with a critical wave number of 2 for the case with constant heat flux at the upper surface $Nu = 0$, Table 1. Equation 15 clearly gives a straight line in the $(N_C - N_T)$ plane for a given set of (Nu, Sh, α). Note that this static stability boundary is independent of Pr and e. The envelope of the family of curves parameterized by the wave number α in Eq. 15 is defined by

$$F = F_\alpha = 0 \tag{16}$$

An analytical expression for this envelope is not possible and we construct the static stability curves numerically from Eq. 16. A typical envelope is shown in Figure 2a with some of the simple bifurcation lines for three different wave numbers α. Above the envelope, some modes are unstable. However, stability is not assured below the envelope, excepting the single-gradient cases on the N_C and N_T axes, since certain modes can still destabilize via a Hopf bifurcation, which is not described by the static boundary Eq. 15. Finally, in Table 1 we list the critical values of N_T and α as a function of Nu for the single driving force case for future reference.

When the leading eigenvalues β (or λ) in the characteristic Eq. 14 are purely imaginary, the convective current is time-periodic with zero growth rate. The Hopf bifurcation curve represents the occurrence of this disturbance in the parameter space. In particular, if we want to locate the Hopf line in the N_C–N_T plane, we can solve the equation

$$\phi(\lambda = i\omega, \alpha, p) = 0 \tag{17a}$$

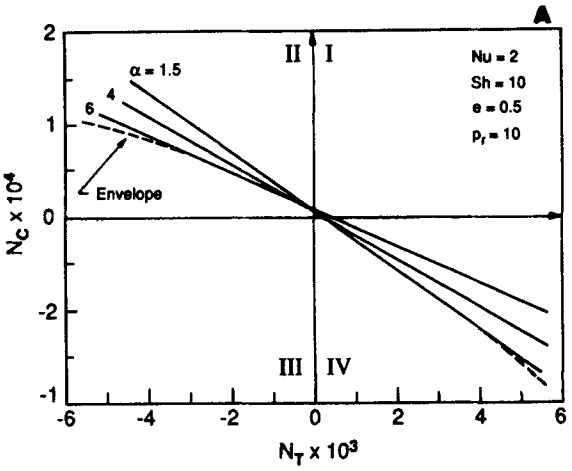

Figure 2a. Static ability lines for several wave numbers α, and envelope of these lines.

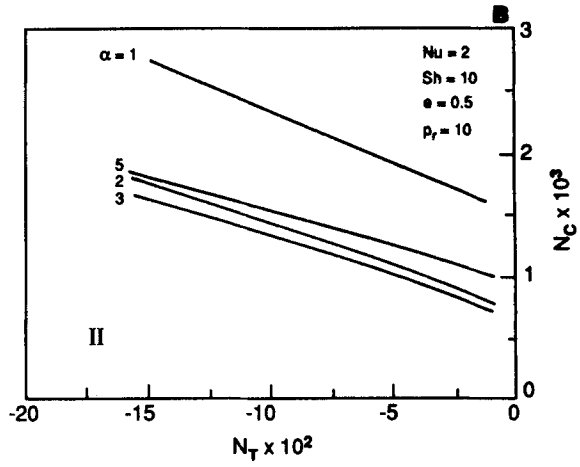

Figure 2b. Oscillatory stability boundaries for several wave numbers α.

Note that these Hopf lines do not cross and are bounded from below by the line for $\alpha_c = 2.69$

that is,

$$Re(\phi) = Im(\phi) = 0 \tag{17b}$$

for (N_T, N_C) as ω increases from zero. The vector p denotes all system parameters. Figure 2b depicts several Hopf lines at various values of α. We are interested in the lowest Hopf curve which gives the critical oscillatory stability boundary. In other words, this is the Hopf curve for the most critical wave number α_c that destabilizes first as one traverses the Marangoni parameter space. It is found numerically that $\alpha_c = 2.69$ when $Nu = 2$, $Sh = 10$, $Pr = 10$, and $e = 0.5$. (This will be our standard case in all subsequent computations.) To demonstrate this oscillatory onset of the Marangoni instability more explicitly, we plot the dispersion curves $Re(\lambda)$ vs. α as N_C crosses the stability boundary at constant N_T in Figure 3. It is seen from the dispersion curves that the instability curves at $\alpha \approx 2.69$ at the critical value of $N_C \simeq 716.6$.

The stable region in the Marangoni parameter space is demarcated by the envelope of static boundaries and the critical

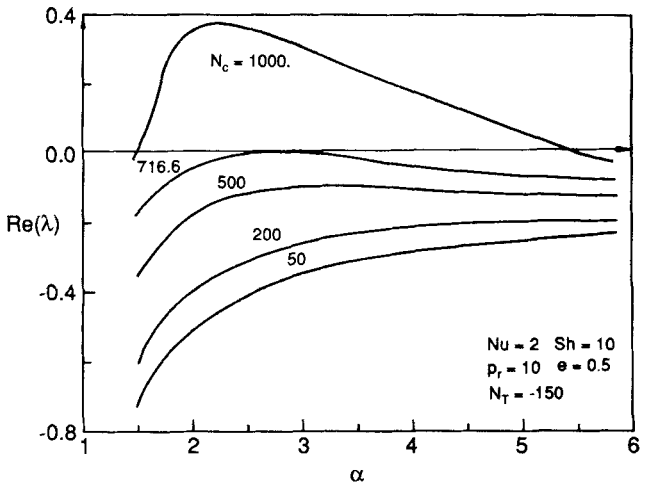

Figure 3. Dispersion curve relating growth rate (real part of leading eigenvalue) to wave number for several solute Marangoni numbers N_C.

Destabilization occurs at a finite critical wave number $\alpha_c = 2.69$; as shown in Figure 2b, this critical wave number is independent of the temperature Marangoni number N_T

Hopf boundary defined above. These two curves are depicted in Figure 4 for the standard case. The region below both curves is stable. If one exits this stable region across the critical Hopf line, oscillatory instability ensues with wave number $\alpha_c = 2.69$. On the other hand, if one traverses the Marangoni parameter space and exits the stable region at the static envelope, static instability results and the resulting stationary rolls have a wave number that is dependent on the exact point of crossing. Hence, unlike the Hopf crossing, the critical static wave number varies along the envelope. This has an important physical implication. The ability of steady convective cells to increase their size provide a mechanism for sustaining convection with the minimum of viscous dissipation. The oscillatory cells are not given this possibility. Hence, one expects the steady roll cells to dominate over the oscillatory ones as the steady critical wave number decreases. This is indeed the case as one compares Figure 2 to Figure 4.

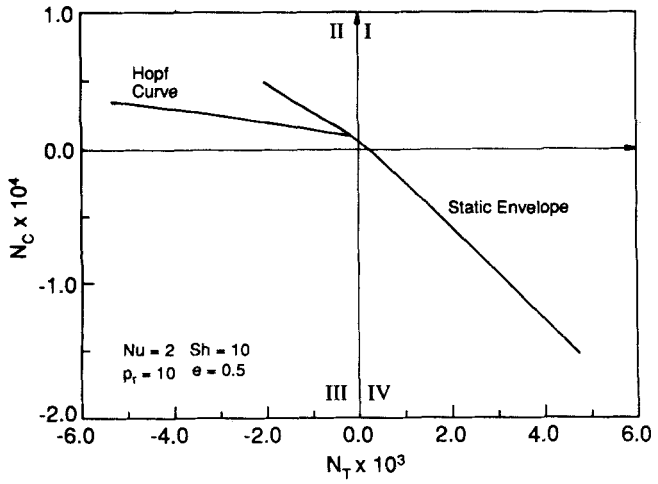

Figure 4. Combined static envelope and critical oscillatory boundary which demarcate the stable region of the Marangoni parameter space.

In the nonlinear analysis, it is convenient to choose the critical oscillatory wave number α_c and impose this spatial periodicity even for the static stability boundary. This implies that the static envelope of Figure 4 will be replaced by the static stability boundary corresponding to α_c. This is shown in Figure 5. Note from Figures 5 and 6 that the error introduced by this approximation is small. This is because the static stability boundaries tend to be very close to each other, yielding an almost straight-line envelope, as is evident in Figure 2a. One nonlinear problem we will address is the finite-amplitude instability of the base states. If the convective rolls bifurcate subcritically, which will be shown to occur, the linearly stable region depicted in Figure 5 does not represent nonlinear or global stability. Large-amplitude disturbances can cause the system to collapse into convective rolls even though the base state is linearly stable. This and the accompanying hysteresis phenomenon have been observed in the closely analogous doubly-diffusive Benard problem by Caldwell (1970), Legros et al. (1970) and Platten and Chavepoyer (1972).

We also note that the Hopf line emanates from the simple line in Figure 5 at a point A_0 where the frequency ω of the imaginary eigenvalue vanishes exactly. This will be referred to as the double-zero singularity. Since it represents the junction of the Hopf and simple curves, one expects complex dynamics in its vicinity due to interactions between the periodic and stationary solutions. These two modes will compete for dominance. This will in fact be revealed in a subsequent bifurcation analysis which uncovers a heteroclinic orbit solution that corresponds to a time-dependent roll cell with an infinite period.

To study the necessary condition for the onset of oscillatory instability, we note from the proof of Vidal and Acrivos (1966) that the oscillatory stability boundary cannot intersect the N_T and N_c axes in the Marangoni plane. We also note that the Hopf lines emanate from the double-zero singularities on the simple lines (A_0 in Figure 5). Hence, the Hopf lines will appear in the same quadrants of the N_T–N_c plane as the double-zero singularities. However, the double-zero singularity corresponds to when

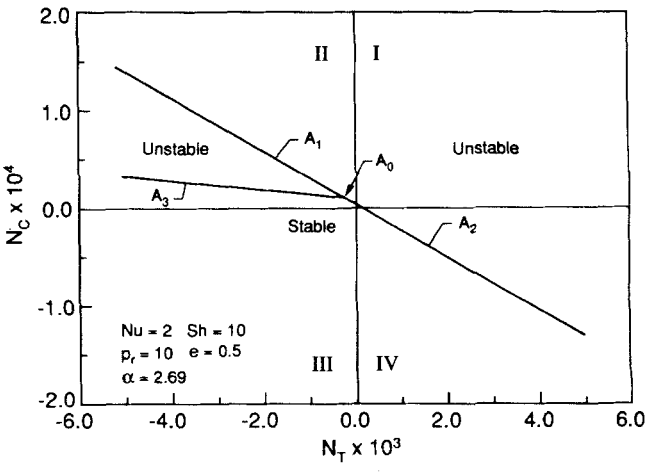

Figure 5. Stable region if wave number α_c of the critical oscillatory stability boundary is imposed even for the static instability.

Instead of the envelope of all static boundaries, the one corresponding to α_c is used
Standard parameter values: $Nu = 2$; $Sh = 10$; $Pr = 10$; $e = 0.5$

the characteristic Eq. 14 has a zero root of multiplicity 2:

$$\phi(\lambda = 0) = \phi'(\lambda = 0) = 0.$$

Note that the first equation, $\phi = 0$, defines the straight simple line, Eq. 15, and is independent of e and Pr as we noted earlier. The second equation, $\phi' = 0$, is also a straight line in the Marangoni plane, as is evident from Eq. 14. The intersection of these two straight lines yields the double-zero singularity. (There is hence a unique double-zero singularity.) We now focus on the parameter e, which is bounded in the interval $(0, \infty)$. It is clear from Eq. 14 that at $e = 0$, $\phi' = 0$ defines the straight line $N_c = 0$, whereas at $e = \infty$, $\phi' = 0$ becomes $N_T = 0$. Inasmuch as Eq. 15 is invariant to the value of e, this implies that at the extreme values of $e = 0$ and ∞, the double-zero singularity lies at $(N_T, N_c) = (0, N_C^c)$ and $(N_T^c, 0)$ where N_C^c and N_T^c are the single-gradient critical Marangoni numbers listed in Table 1. These two points bound the segment of the simple line in the first quadrant. We shall then demonstrate numerically that for $e\epsilon(0, \infty)$, the double-zero singularity lies in either the second or fourth quadrant where N_T and N_C are of opposite signs. This is shown in Figures

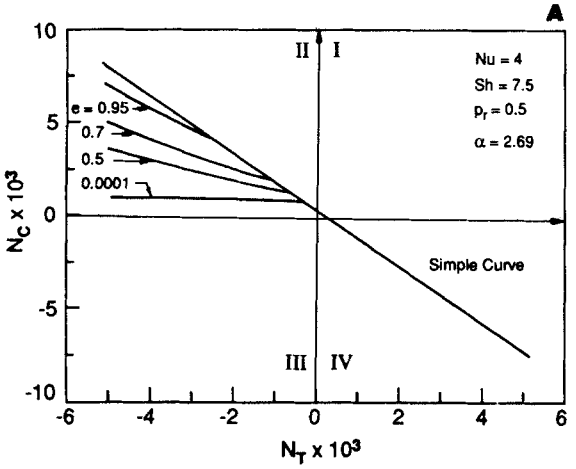

Figure 6a. Oscillatory stability boundary in the second quadrant.

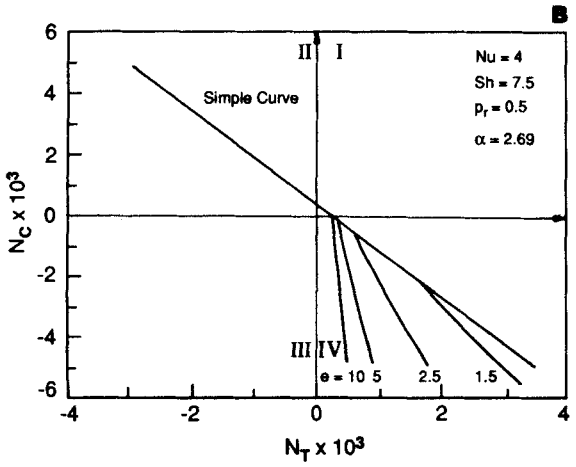

Figure 6b. Oscillatory stability boundary in the fourth quadrant.

6a and 6b where the double-zero is shown to jump from one infinity end of the simple line in the second quadrant to the other infinity end in the fourth quadrant. The critical e where this occurs corresponds to when the two straight lines, $\phi = \phi' = 0$, have identical slope in the Marangoni plane and it is a complex function of Nu, Sh, and Pr. When $Nu = Sh$, however, simple symmetry arguments demonstrate that this critical e is unity. We have hence shown that the double-zero is bounded away from the segment of the simple line in the first quadrant and hence must lie on the remaining segment of the simple line in the second and fourth quadrants. Equivalently, oscillatory instability exists either in the second or the fourth quadrants where the Marangoni numbers have opposite signs. It appears in the quadrant where the destabilizing driving force is dominant. For example, for $e > 1$ the thermal diffusivity is larger and the temperature gradient is dominant. Hence, oscillatory instability occurs in the fourth quadrant where $N_T > 0$ is destabilizing.

It must be pointed out that for typical chemical Marangoni instability, concentration fluctuations are far more dangerous than thermal, velocity, density (buoyancy), or electrical potential fluctuations because of their relatively long lifetime. A small concentration gradient can trigger convective current. This can be seen from the above linear analysis by realizing that the solutal Marangoni numbers are extremely large even for moderate concentration gradient due to the smallness of the diffusivity D relative to the thermal diffusivity κ. Hence, even when one has a large stabilizing thermal gradient ($N_T < 0$), a slight destabilizing concentration gradient ($N_C > 0$) can cause oscillatory instability, Figure 6a. On the other hand, when the solutal gradient is stabilizing ($N_C < 0$), one must impose a large destabilizing temperature driving force to cause convective rolls. This has been pointed out by Berg and Acrivos (1965), who suggested that surface-active agents which reduce surface tension may (even in trace amounts) have a strong stabilizing effect on air-liquid interfaces.

From Figures 2 to 6, one can deduce several rules of thumb regarding the stability of the interface:

1. Increasing viscosity and decreasing the film thickness stabilizes the film due to increased viscous dissipation. These effects reduce the Marangoni numbers N_T and N_C and increase the Prandtl number Pr. Note that Pr affects the oscillatory boundary but not the static boundary.

2. The closer the Lewis number e is to unity, the more stable the interface. This is because oscillatory instability is induced by the two opposing gradients in quadrants II and IV (where N_T and N_C are of opposite signs). When e is much less than or much greater than unity, the stabilizing species becomes extremely slow and ineffective. Note that e does not induce static instability.

3. Increasing fluxes to the gas phase by increasing the local Nusselt Nu and Sherwood Sh numbers stabilizes the interface. This is evident from Eq. 15. Physically, enhanced transfer to the gas phase diminishes the interfacial gradient when the gradient is destabilizing. It increases interfacial gradient when it is stabilizing.

4. The strong stabilizing/destabilizing effects of surfactants are felt at the maximum growing wave number region, Figure 3, where the wavelengths are approximately equal to the thickness of the liquid film. This is in contrast to the weak stabilizing effects of surfactants on gravity-capillary waves of most liquid jets. For liquid jets, the surfactants only damp out the inconse-

quential ripples, which are far shorter than the maximum growing disturbances with wavelengths the order of the jet radius (Levich, 1981).

5. Under almost all physical conditions, the wavelength of the roll waves is about two to three times the film thickness. This is due to the insensitivity of α_c to the physical parameters.

Jacobi-Tau Spectral Method

We shall tackle the fully nonlinear problem with a modified spectral method. In a classical global Galerkin/spectral method, the approximated solution is expanded in a series of basis functions for discretization purposes. Each basis function satisfies all the boundary conditions exactly. However, it is impossible to construct basis functions that satisfy the free-surface boundary conditions at $z = 1$, Eqs. 8e–8h, in the present problem. This is remedied by a special tau expanion described by Gottlieb and Orszag (1977) that retains these troublesome boundary conditions as additional algebraic equations and increases the number of expansions to exactly satisfy the correct degree of freedom.

We first expand the dependent variables ψ, S, and G in terms of the Jacobi polynomials $P_N^{(\alpha,\beta)}(z)$. In choosing the appropriate Jacobi polynomials, we take into consideration the following factors. The expansions are premultiplied by certain factors such that all boundary conditions except the more complex heat, mass, and momentum balance conditions at the free surface are satisfied automatically. These same factors will then determine the weighting functions of the Jacobi polynomials since we prefer basis functions that are orthogonal with respect to inner products that include these weighting functions. There are two reasons for this. Orthogonal bases are often the most optimal linearly independent basis set for numerical purposes. More importantly, a major advantage of spectral methods is the ability to convert partial differential equations(s) (PDE) into the form $\boldsymbol{x}_t = \boldsymbol{f}(\boldsymbol{x})$, which is most amenable to bifurcation analysis. Other numerical schemes, such as finite-elements or finite-difference, can also achieve this but with considerable more effort. However, in projecting the PDE to the above form, a "capacitance matrix" involving inner products of the terms containing partial derivatives with respect to time usually needs to be inverted numerically. This is especially true in the tau method since some of the boundary conditions yield equations that must be solved algebraically. Orthogonal bases usually yield diagonal or block-diagonal capacitance matrices that can be inverted easily. Since such matrices are usually or large dimensions and their inversion is a major numerical obstacle, orthogonal bases which facilitate the inversion are extremely desirable.

Considering these factors, the final expansions chosen are, (Ho, 1987),

$$\psi(x, z, t) = \sum_{i=1}^{M}\sum_{j=0}^{N} a_{ij}(t)\, \phi_j(z) \sin(i\alpha_c x) \tag{18a}$$

$$S(x, z, t) = \sum_{i=0}^{M}\sum_{j=0}^{N} b_{ij}(t)\, \eta_j(z) \cos(i\alpha_c x) \tag{18b}$$

$$G(x, z, t) = \sum_{i=0}^{M}\sum_{j=0}^{N} c_{ij}(t)\, \eta_j(z) \cos(i\alpha_c x) \tag{18c}$$

where

$$\phi_j(z) = z^2(1 - z)P_j^{(2,4)}(z) \tag{18d}$$

$$\eta_j(z) = zP_j^{(0,2)}(z) \tag{18e}$$

We first substitute Eq. 18a into Eq. 7a, multiply the resulting equation by $\phi_k(z) \sin(\ell\alpha_C x)$, and then integrate from $x = 0$ to π/α_c, $z = 0$ to 1. Similarly, we substitute Eq. 18 into Eqs. 7b and 7c, multiply the resulting equations by $\eta_k(z) \cos(m\alpha_c x)$, and integrate over the same domain. Note that $k = 0, 1, 2, \ldots, N - 1$, $\ell = 1, 2, \ldots, M$, and $m = 0, 1, 2, \ldots, M$. This is the major difference between the tau method and the Galerkin/spectral method. The latter method requires $k = 0, 1, 2 \ldots, N$ instead. The above computations lead us directly to the following system of ODE's:

$$\boldsymbol{\Omega}\frac{d\boldsymbol{a}}{dt} = \boldsymbol{\Xi a} + \boldsymbol{a}^T\boldsymbol{\Gamma a}, \tag{19a}$$

$$\boldsymbol{\Pi}\frac{d\boldsymbol{b}}{dt} = \boldsymbol{K a} + \boldsymbol{H b} + \boldsymbol{a}^T\boldsymbol{\Sigma b}, \tag{19b}$$

$$\boldsymbol{\Pi}\frac{d\boldsymbol{c}}{dt} = \boldsymbol{K a} + \theta\boldsymbol{c} + \boldsymbol{a}^T\boldsymbol{\Sigma c}, \tag{19c}$$

where $\boldsymbol{a}^T = [a_{11} \ldots a_{1N} a_{21} \ldots a_{2N} \ldots a_{MN}]$, $\boldsymbol{b}^T = [b_{01} \ldots b_{0N} b_{11} \ldots b_{MN}]$, etc. The definitions and dimensions of matrices and tensors are given in Ho's thesis. It should be noted that the capacitance matrix is block-diagonal, containing submatrices $\boldsymbol{\Pi}$, which is diagonal, and $\boldsymbol{\Omega}$. These submatrices are independent of any system parameter (except α_c). The other matrices and tensors are parameter-dependent. Very conveniently, however, all pertinent inner products need only be evaluated once for all parameter values. It is clear that Eqs. 19 represent a system of $N(3M + 2)$ equations and $(N + 1)(3M + 2)$ unknowns. In order to solve the problem, we need an additional $(3M + 2)$ equations. This is done by substituting Eq. 18 into the remaining boundary conditions of Eqs. 8f to 8h, and performing the appropriate inner products. The additional $(3M + 2)$ equations are linear with respect to the coefficients of the additional $(3M + 2)$ bases since the problematic boundary conditions, Eqs. 8f to 8h, are linear. After a simple inversion to solve for these coefficients in terms of the other $N(3M + 2)$ bases and substituting into Eq. 19 (for details see Ho's thesis) a single set of first-order ODE's, which represents a tau-spectral projection of the original infinite dimensional problem in Eqs. 7–9, results. These $N(3M + 2)$ equations are only quadratic in the expansion coefficients $\boldsymbol{u} = (\boldsymbol{a}, \boldsymbol{b}, \boldsymbol{c})$ due to the original quadratic nonlinearity J in Eq. 6. After an inversion of the capacitance matrix, the projected equations appear in the requisite form,

$$\frac{d\boldsymbol{u}}{dt} = \boldsymbol{L u} + \boldsymbol{u X u} \tag{20}$$

where the tensors $\boldsymbol{L}$ and $\boldsymbol{X}$ are dependent on the six system parameters N_T, N_C, Pr, e, Sh, and Nu. All the pertinent inner products in the construction of $\boldsymbol{L}$ and $\boldsymbol{X}$ involve a double integral over $(0, 1)$ in the z direction and $(0, \pi/\alpha_c)$ in the x direction. The integration is simple for our box geometry. It is especially

trivial for the x direction due to the orthogonality of the Fourier series. In fact, all the integrals in the x direction are analytically evaluated. Integration in the z direction involves products of various families of Jacobi polynomials with certain weighting factors. We evaluate these integrals by using orthogonal collocation as described by Villadsen and Michelson (1978). In particular, their package programs JCOBI and DFOPR are used. The idea is to evaluate the weighting factors w_i at the collocation points x_i in the formula:

$$\int_0^1 x^\beta (1-x)^\alpha R_N(x)dx = \sum_{i=1}^{n} w_i R_N(x)$$

where $R_N(x)$ is any polynomial of degree less than or equal to $2n-1$. In order to evaluate the integral exactly, the collocation points x_i are chosen to be the zeros of the Jacobi polynomial $P_n^{(\alpha,\beta)}(x)$. Depending on the degree of $R_N(x)$, on the average each integral takes approximately 2.5 s CPU time on a VAX 780 computer. A total of 1,452 integrals need to be evaluated for a given set of parameters to fully specify Eq. 20.

The convergence of the Jacobi-tau method is tested by computing the leading eigenvalue(s) of the matrix L, its size $I = N(3M+2)$ increases, and comparing them to the exact neutral eigenvalues computed in the Orr-Sommerfeld analysis. Since the M horizontal modes are linearly decoupled, we fix the maximum horizontal mode number M at 2, and increase the maximum vertical mode number N. Increasing M would not alter the eigenvalues of the lower horizontal modes. In particular, we choose points from the exact stability boundaries A_0, A_1, A_2, and A_3 in Figure 5 and examine the convergence of the numerical eigenvalues to the exact ones which have vanishing real parts. Figure 7 summarizes the results in our convergence tests. It can be seen that in each case exponential convergence is obtained. The convergence is excellent (exponential with large decay rate) for both the Hopf curve and the simple curve. On the other hand, because of higher singularity at the double-zero point, the convergence of the two leading zeros is not as sharp. The flat tails at the end are because we have reached the limit of machine accuracy for further increase of I. It is easily seen that for $I = 80$, the eigenvalues are estimated to be correct to the eighth decimal place. We shall hence assume that for $I = 80$, the nonlinear PDE will also be as accurately estimated. Finally, in Table 2 we list the eigenvalues at the simple bifurcation point for the case of a single driving force with $Nu = 2$, and $Pr = 10$.

Normal Form Bifurcation Analysis

In the previous section we demonstrated the validity of the Jacobi-tau spectral method for the present free-surface problem. One can, in principle, construct the roll cell solutions that should replace the purely diffusive and conductive base state in Eqs. 2 for regions in the parameter space where the base state is unstable. The net heat and mass fluxes for these roll cells, which should be greater than those at the base state, can also be computed. However, since there is a total of six parameters, Nu, Sh, Pr, e, N_T, and N_C, an exhaustive numerical search is both tedious and unproductive. Hence, while we shall carry out some judicious numerical construction of heat and mass transfer enhancement, we will focus our attention on regions near the stability boundaries. In particular, the double-zero singularity A_0 at the junction of the Hopf and simple loci and the simple curve itself

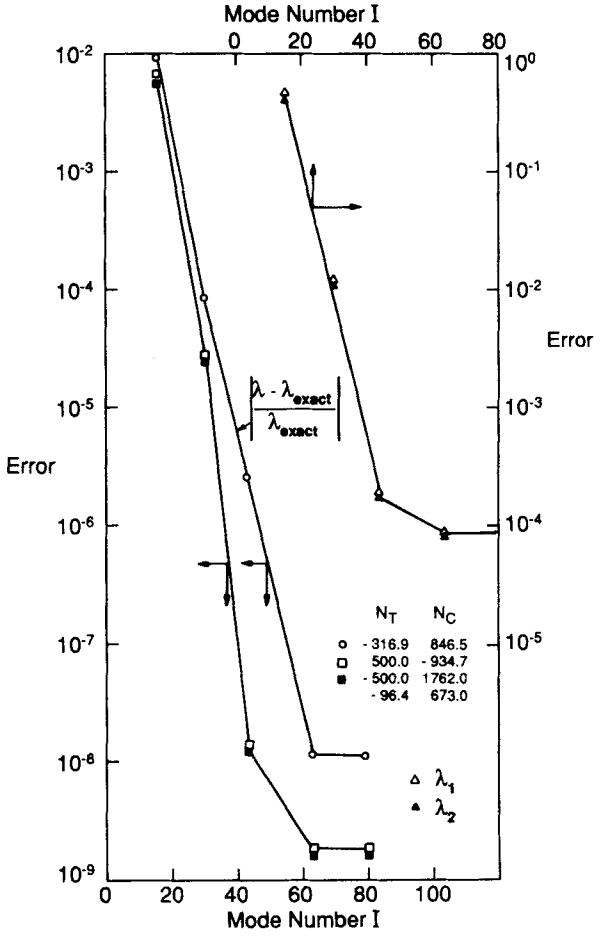

Figure 7. Numerical convergence test for marginally stable eigenvalues on boundaries shown in Figure 5.

O Oscillatory stability boundary A_3
□ Static stability boundary A_2
■ Static stability boundary A_1
△▲ Double-zero singularity A_0

Table 2. Eigenspectrum at the Simple Bifurcation Point for a Single Driving Force ($Nu = 2$, $Pr = 10$)

0.0	−20.393110
−0.523919	−20.955824
−1.639093	−22.330604
−1.754384	−23.597690
−2.587741	−23.662994
−3.086313	−27.390473
−3.274171	−28.837693
−5.179899	−30.279829
−6.554785	−30.941406
−6.636805	−33.179353
−7.427973	−33.542933
−7.700005	−43.451579
−8.084025	−43.563144
−9.629735	−44.898799
−12.425685	−45.352528
−12.482904	−46.112027
−13.491008	−47.959064
−15.166944	−49.240459
−15.650932	−62.729391
−16.614164	−63.445331

Note that only the first 40 eigenvalues are shown.

will be examined. We shall also use the center manifold theory and the normal form analysis in this section to construct a locally correct and convenient expression for the enhancement factor in the vicinity of the simple curve.

The power of this bifurcation analysis is not limited to the construction of such correlation-like expressions for the enhancement factors. In fact, it also offers a qualitatively correct description of the dynamic portraits near the bifurcation points, that is, classification of "dynamic portraits." For example, in the case of the simple bifurcation curve, we shall demonstrate that the stationary roll cells appear beyond the bifurcation points (supercritical bifurcation) in the first quadrant of the Marangoni number space. Hence, finite-amplitude instability is not possible for the linearly stable base states. This is not true, however, when the gradients are opposite. The roll cells can appear before the simple bifurcation points (subcritical bifurcation). Hence, in the first quadrant, the roll cell solutions can only be found in regions of the parameter space where the nonconvective base state is unstable. In the second and fourth quadrants, however, they can appear before the base state loses its stability, Figure 11. Similarly, normal form analysis about the double-zero singularity also reveals certain unexpected dynamic behavior. Since the Hopf and simple lines coalesce at this singularity, one intuitively expects that the time-periodic solutions which bifurcate from a Hopf line and the steady-state solutions which bifurcate from a simple line will somehow interact (compete for dominance) near this singularity. In fact, a heteroclinic orbit is born near this point that is not found near a simple or Hopf point otherwise. At this point, when the steady rolls annihilate the oscillatory rolls, an oscillatory roll with an infinite period of oscillation occurs—a unique phenomenon that can easily be detected.

We shall begin by deriving the amplitude equations about the double-zero point A_0 of Figure 5. We shall assume initially that the tensors in Eq. 20 are evaluated at the double-zero point and that we are interested in the dynamics at that point. Hence, $\boldsymbol{L}$ contains two zero eigenvalues of degeneracy one. The generalized eigenvector y_1' for these repeated eigenvalues is computed by Gaussian elimination on $\boldsymbol{L}y_1' = y_1$, where $\boldsymbol{L}y_1 = 0$. All the other eigenvalues and eigenvectors are evaluated from subroutine EIGZF available from the IMSL library. These eigenvectors are used to construct the transform matrix $\mathrm{P} = [y_1 y_1' y_2 \ldots y_l]$. Let $\boldsymbol{v}$ be the transformed vector, that is, $\boldsymbol{u} = \boldsymbol{P}\boldsymbol{v}$. The set of ODE's in Eq. 20 is transformed into the form

$$\frac{d\boldsymbol{v}}{dt} = \boldsymbol{\Lambda}\,\boldsymbol{v} + \boldsymbol{v}^T\,\boldsymbol{\Pi}\,\boldsymbol{v} \tag{21}$$

where $\Pi_{ijk} = (\boldsymbol{P}^{-1})_{jl}(\boldsymbol{P}^T\boldsymbol{X}\boldsymbol{P})_{ilk}$, and $\boldsymbol{\Lambda}$ is an $I \times I$ matrix:

$$\boldsymbol{\Lambda} = \begin{pmatrix} \boldsymbol{A} & 0 \\ 0 & \boldsymbol{B} \end{pmatrix} \tag{22}$$

in which $\boldsymbol{B}$ is a $(I-1) \times (I-1)$ matrix in Jordan form with all the nonzero eigenvalues, and $\boldsymbol{A}$ is a 2×2 matrix simply given by

$$\boldsymbol{A} = \begin{pmatrix} 0 & 1 \\ 0 & 0 \end{pmatrix} \tag{23}$$

Hence Eq. 21 can also be written in the form:

$$\frac{d\boldsymbol{x}}{dt} = \boldsymbol{A}\boldsymbol{x} + \boldsymbol{f}(\boldsymbol{x}, \boldsymbol{y}) \tag{24a}$$

$$\frac{d\boldsymbol{y}}{dt} = \boldsymbol{B}\boldsymbol{y} + \boldsymbol{g}(\boldsymbol{x}, \boldsymbol{y}) \tag{24b}$$

where $\boldsymbol{x}$ are simply the two neutral modes at the double-zero singularity.

Since the two leading eigenvalues of Eqs. 24 vanish exactly, it is clear that the dynamics about the origin fixed point, which corresponds to the stationary base state, cannot be resolved by linearization. The nonlinear dynamics also seems formidable due to the large dimensions. Fortunately, the center manifold theorem allows a drastic reduction of dimension at a bifurcation point, such as the present double-zero singularity. The center manifold is an invariant manifold in the state space from which trajectories will never escape. It is tangent to the eigenspace spanned by y_1 and y_1' near the origin fixed point. The center manifold theorem (Holmes, 1981) then states that there is a local, nonlinear transformation of $\boldsymbol{x}$ and $\boldsymbol{y}$ such that the transformed stable modes decay exponentially and the nonlinear dynamics are governed only by the equations for the center manifold. In our case, the center manifold is two-dimensional and hence the projected equations that contain all the dynamics are only two-dimensional. We use the center manifold projection technique of Carr (1981, 1983), and derive the coefficients of the transformation (projection) in the Appendix. It involves expressing v_3 to v_1 as $0(2)$ functions of v_1 and v_2. The projected equations for the center manifold are

$$\frac{dv_1}{dt} = v_2 + A_1 v^3 + B_1 v_1^2 v_2 + C_1 v_1 v_2^2 + D_1 v_2^3 + 0(|v_1|^5, |v_2|^5) \tag{25a}$$

$$\frac{dv_2}{dt} = A_2 v_1^3 + B_2 v_1^2 v_2 + C_2 v_1 v_2^2 + D_2 v_2^3 + 0(|v_1|^5, |v_2|^5) \tag{25b}$$

Detailed calculations and definitions of the coefficients in Eqs. 25 are given in the Appendix. Note that due to the symmetries of the nonlinear J terms in Eq. 7, only odd terms remain in the projected equations.

Equations 25 are still too complicated to analyze. Further simplification can be made by transforming $\boldsymbol{v}$ with some analytic, nonlinear transformation that eliminates certain terms. (These terms are actually transformed into higher order terms.) Since the transformation is diffeomorphic, it does not alter the dynamics. There are, however, certain nonresonant terms that can never be removed. These terms for the present double-zero singularity are well documented in the literature (Guckenheimer and Holmes, 1983). In our case, the normal form does not have second-order terms; the only nonresonant cubic terms are v_1^3 and $v_1^2 v_2$ in the second equation. Hence, by Taylor-expanding the near-identity transformation,

$$z_1 = v_1 + Q_1(v_1, v_2), \quad \text{and} \quad z_2 = v_2 + Q_2(v_1, v_2) \tag{26}$$

and setting the coefficients for the other terms in the trans-

formed equations to zero, one can obtain the coefficients for the transformation as well as the transformed equation. (Taylor coefficients of the transformation are tabulated by Hwang and Chang, 1987.) The transformed equations are

$$\frac{dz_1}{dt} = z_2 \tag{27a}$$

$$\frac{dz_2}{dt} = \alpha_1 z_1^3 + \alpha_2 z_1^2 z_2 \tag{27b}$$

where $\alpha_1 = A_2$, $\alpha_2 = B_2 + 3A_1$. This Arnold's normal form is equivalent to the nonlinear oscillator equation

$$\frac{d^2z_1}{dt^2} - \alpha_1 z_1^3 - \alpha_2 z_1^2 \frac{dz_1}{dt} = 0 \tag{28}$$

Its phase portrait has been extensively analyzed in the literature (Holmes, 1981) and the origin is a degenerate saddle point depicted in the origin of the ϵ_1–ϵ_2 parameter space in Figure 8. The dynamics at the double-zero singularity has therefore been deciphered. It contains a base state (the stagnant film) that is nonlinearly unstable (recall that it is linearly neutrally stable with two leading null eigenvalues). Locally, there are also no other new solutions such as fixed points (stationary convective rolls) or limit cycles (time-periodic convective rolls). These new solutions appear away from the double-zero point and we shall now "unfold" the dynamic portraits in its neighborhood in the Marangoni parameter space N_T–N_C. In particular, we note that certain generic unfolding, "versal unfoldings," have been analyzed in the literature. For our problem–a double-zero with odd symmetry–Carr (1981), Holmes (1981), Guckenheimer and Holmes (1983), Guckenheimer and Knobloch (1983), and Nagata and Thomas (1986) have all analyzed certain unfoldings and classified the dynamics for their particular perturbations. We shall hence transform our equations to their particular structures and simply use the results of their analyses. This is one of the advantages of normal form analysis: once it is converted to a literature form, all subsequent results are readily available without further analysis.

Away from the double-zero singularity, one can write Eq. 20 as

$$\frac{du}{dt} = (L_0 + L^1)\, u + u^T (X_0 + X^1) u \tag{29}$$

where the subscript zero denotes evaluation at the double-zero and superscript ′ in the following equations denotes deviation away from the singularity. Using the same similarity transform P at the double-zero, Eq. 29 can be converted to

$$\frac{dv}{dt} = (\Lambda_0 + \Lambda')\, v + v^T(\Pi_0 + \Pi')v \tag{30}$$

The primed tensors and matrices contain the deviation terms from the double-zero and, assuming small deviations, they contain elements of order ϵ. Note that Λ' is not in a Jordan form since the similarity transform is only appropriate for L_0 at the double-zero point. Next, we assume that we apply the same center manifold projection of the unperturbed system (the validity of this is proven in Guckenheimer and Holmes, 1983) and obtain, without explicit construction, the perturbed version of Eqs. 25:

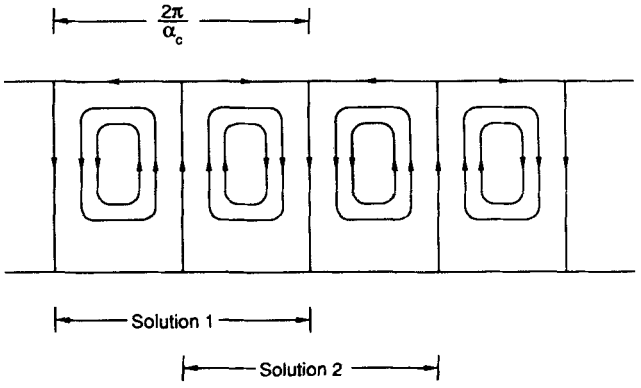

Figure 8. Symmetry of the solutions $v_1 \leftrightarrow -v_1$ corresponds to a phase shift of one half-wavelength.

$$\frac{dv}{dt} = (A_0 + A')v + f_0(v) + f'(v) \tag{31}$$

where

$$A_0 = \begin{pmatrix} 0 & 1 \\ 0 & 0 \end{pmatrix}$$

and A' and f' denote the contribution from perturbation away from the double-zero singularity. It is clear that A' is of $0(\epsilon)$ and f' is $0(\epsilon|v|^3)$. Since f_0 is $0(|v|^3)$, one can hence neglect f' entirely. This implies that one could use the nonlinear terms of Eqs. 25 in the perturbed equation without altering *qualitatively* the dynamics. The quantitative effect is also only of $0(\epsilon)$. Also, since the center manifold projection is a nonlinear 0(2) transformation, it does not alter the linear part Λ' of Eq. 30. Hence,

$$A' = \begin{pmatrix} A'_{11} & A'_{12} \\ A'_{21} & A'_{22} \end{pmatrix} \tag{32}$$

This, however, is not an unfolding studied in the literature. One desired form is

$$A' = \begin{pmatrix} 0 & 0 \\ \epsilon_1 & \epsilon_2 \end{pmatrix} \tag{33}$$

and we hence seek to transform away the first row of Eq. 32. This involves a linear transformation,

$$v = (I + B)z \tag{34}$$

where $B \sim 0(\epsilon)$ remains to be determined. This transformation again does not affect the nonlinear terms up to $0(\epsilon)$. However, since there are no v_1 term in the first equation and no v_2 term in the second equation, transformation Eq. 34 will affect these

terms. In fact the matrices to the linear terms of Eq. 31 are transformed as such

$$A_0 + A' \rightarrow A_0 + (A_0 B - B A_0 + A') \tag{35}$$

where we have made use of the relationship to leading order,

$$B \frac{dz}{dt} \sim B \frac{dv}{dt} \sim B A_0 v \sim B A_0 z \tag{36}$$

Hence, we require

$$\begin{pmatrix} 0 & 0 \\ \epsilon_1 & \epsilon_2 \end{pmatrix} = A_0 B - B A_0 + A' = \begin{pmatrix} B_{21} & B_{22} - B_{11} \\ 0 & -B_{21} \end{pmatrix} + A' \tag{37}$$

which yields four equations for the four unknowns ϵ_1, ϵ_2, B_{21}, and $B_{22} - B_{11}$. Note that the matrix B need not be fully specified. The results for ϵ_1 and ϵ_2 are

$$\epsilon_1 = A'_{21} \tag{38a}$$

and

$$\epsilon_2 = A'_{11} + A'_{22} \tag{38b}$$

Hence, in summary, the nonlinear dynamics about the double-zero singularity is described qualitatively up to $0(\epsilon)$ by the following perturbed normal form amplitude equation:

$$\frac{dz_1}{dt} = z_2 \tag{39a}$$

$$\frac{dz_2}{dt} = \epsilon_1 z_1 + \epsilon_2 z_2 + \alpha_1 z_1^3 + \alpha_2 z_1^2 z_2 \tag{39b}$$

where $\alpha_1 = A_2$, $\alpha_2 = B_2 + 3A_1$ as in the unperturbed normal form. The coefficients A_1, A_2, and B_2 are the same as in Eq. 25 and are obtained numerically from the full equations after the center manifold projection. The perturbed parameters ϵ_1 and ϵ_2 are evaluated from

$$\Lambda' = P^{-1} J P \tag{40}$$

where

$$J = \delta N_T \frac{\partial L}{\partial N_T} + \partial N_C \frac{\partial L}{\partial N_C} \tag{41}$$

Note that L is the full $I \times I$ (or 80×80) Jacobian and

$$\begin{aligned} \delta N_T &= N_T - N_T^0 \\ \delta N_C &= N_C - N_C^0 \end{aligned} \tag{42}$$

where N_T^0 and N_C^0 are the locations of the double-zero singularity A_0 in Figure 5. The partial derivatives in Eq. 41 are evaluated numerically using forward difference in the Marangoni parameter space N_T–N_C.

Although we have undergone a finite-dimensional tau-spectral projection, a diagonalizing similarity transform, a center manifold projection, and a normal form analysis in going from the original Eq. 7 to the amplitude equations of Eq. 39, many qualitative features are retained. The conductive and diffusive base state is given by $z_1 = z_2 = 0$. The z_1 and z_2 modes are the two neutrally stable modes at the double-zero singularity A_0. If a time-periodic solution (limit cycle) exists for Eq. 39, a finite-amplitude oscillatory cell appears in the original problem. If another fixed point other than the origin exists for Eq. 39, a steady roll cell exists for the original problem. In fact, due to the symmetry of the steady state version of Eq. 39 to the transformation $z_1 \rightarrow -z_1$, any fixed point $(z_1^*, 0)$ has a companion $(-z_1^*, 0)$. Hence, all steady bifurcations are "pitchfork" bifurcations. The sign of the first mode z_1 corresponds to the sign of the stream function, and hence the two branches of the pitchfork correspond to two roll cells that are rotating in opposite directions. (In fact, they are mirror images of each other.) As shown in Figure 8, one is just a phase shift of the other in a periodic train of roll cells. Consequently, the two solutions are physically indistinguishable and yield identical overall heat and mass fluxes.

The dynamics of the general unfoldings of Eq. 39 has been studied by Guckenheimer and Knobloch (1983); we shall simply cite their results here. For nondegenerate cases, α_1 and α_2 are both nonzero, and the phase portraits around the double-zero point depend only on the signs of α's. Figures 9a and 9b show the cases when $\alpha_1 > 0$, $\alpha_2 < 0$, and $\alpha_1 < 0$, $\alpha_2 < 0$, respectively. With a simple rescaling, the pictures for other cases can readily be obtained. If $Nu = 2$, $Sh = 10$, $Pr = 10$, $e = 0.5$, and $\alpha_c = 2.69$, our numerical computations show that $\alpha_1 = 0.5074 > 0$ and $\alpha_2 = -0.8523 < 0$. And Eqs. 38 lead directly to $\epsilon_1 = (2.397\delta N_T + 0.889\delta N_C) \times 10^{-2}$ and $\epsilon_2 = (5.579\delta N_T + 6.870\delta N_C) \times 10^{-3}$. In this case, if we fix $\delta N_C > 0$ and slowly increase δN_T from negative to positive, the amplitude of the limit cycle (oscillatory convection) increases until (ϵ_1, ϵ_2) hits L_2 of Figure 9a, on which the limit cycle joins the two saddle points to form two heteroclinic orbits. At this time, the oscillation has an infinite period. When δN_T is increased further, the oscillation disappears as the oscillatory mode is annihilated by the steady rolls. Carrying out the linear coordinate transform, the N_C–N_T coordinates are located on the ϵ_1–ϵ_2 plane as shown in Figure 10 such that the classification of the phase portraits around (N_T^0, N_C^0) is now complete for the given parameter values.

It is interesting to find that for various sets of parameters, α_1 is always positive while α_2 is always negative in our numerical computations. In other words, the bifurcation patterns depicted in Figure 9b are not observed in our model. However, this seems to be reasonable according to Nagata and Thomas's (1986) work in which the doubly-diffusive Benard problem of a fluid confined to two horizontal rigid boundaries was considered. In their studies, they were able to prove analytically that for their two-dimensional (roll cell) disturbances, $\alpha_1 > 0$ and $\alpha_2 < 0$ in the Arnold's normal form. Even though we are unable to develop a similar proof for the double-diffusive Marangoni problem, it is reasonable to believe that the same should be true in view of our numerical results.

From the above discussion, it can be seen that our normal form analysis predicts (locally) the occurrence of the subcritical pitchfork bifurcation as one increases N_T and/or N_C across the simple curve near the double-zero in the second quadrant. In the

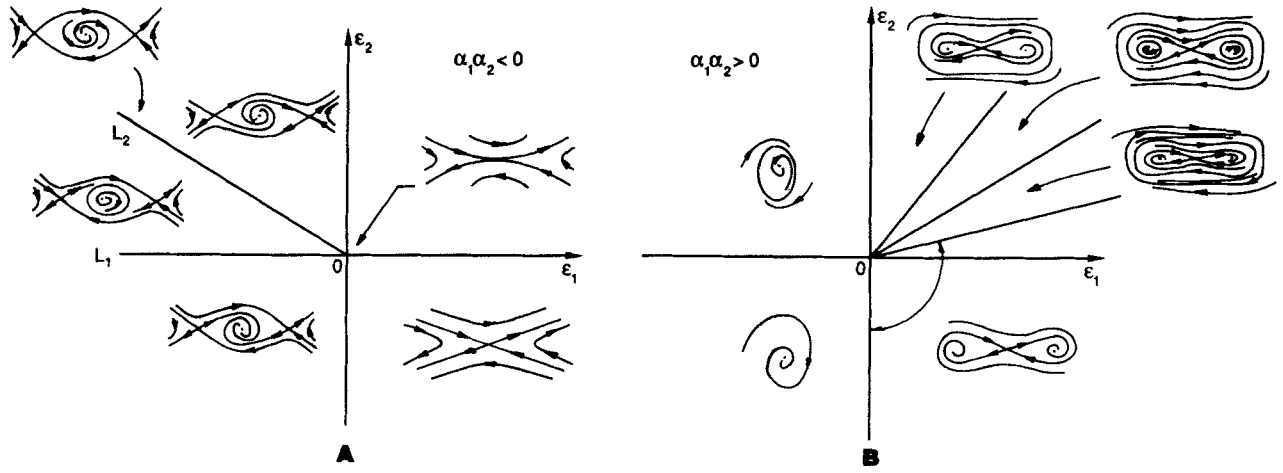

Figure 9. Dynamic phase portraits for the Arnold normal form.
Two unfoldings are possible with α_1 and α_2 of equal or opposite signs

first quadrant, however, one expects a supercritical bifurcation of the steady roll cells. Certainly for the single-component case (N_T or N_C vanishes), one expects the result of Tavantzis for the Benard problem to also be true, that is, supercritical bifurcation of the steady roll occurs whenever the principle of exchange of stability can be established. (Recall that Vidal and Acrivos, 1966, have proven this for the single-component case.) We hence expect the direction of bifurcation to change some place between the N_C axis and the double-zero point in quadrant II. To establish this, we study the direction of bifurcation along the static stability line. In this case, the matrix of transformation is simply $P_0 = [y_1 y_2 \ldots y_l]$. The transformation $u = P_0 v$ brings the linear part of Eq. 20 into Jordan form:

$$\frac{dv}{dt} = \Lambda_0 v + v^T S v \tag{43}$$

where Λ_0 is with a zero leading eigenvalue. With a similar center manifold projection technique (see the Appendix for complete descriptions), we obtain the amplitude equation,

$$\frac{dv_1}{dt} = \epsilon v_1 + \zeta v_1^3 \tag{44}$$

where

$$\epsilon = \delta N_T \frac{\partial A_0}{\partial N_T} + \delta N_C \frac{\partial A_0}{\partial N_C} \tag{45}$$

To determine whether the pitchfork bifurcation is subcritical or supercritical, we need only to check the sign of $\xi = \epsilon\zeta$. If $\xi < 0$, the pitchfork is supercritical, otherwise it is subcritical. In order to simplify our analysis, we choose the x and y intercepts on the simple curve for the analysis. Our numerical results can be summarized as follows for the indicated paths across the simple curve in Figure 11:

Path	Normal Form
B_1	$7.411 \times 10^{-3}\,\delta N_T v_1 - 0.57705\, v_1^3$
B_3	$7.121 \times 10^{-3}\,\delta N_C v_1 - 0.16625\, v_1^3$

Since the signs of ξ's are negative in both cases, the pitchfork is always supercritical in the nonoscillatory region, even though normal form analysis reveals a subcritical pitchfork around the double-zero point. This implies that the direction of bifurcation of the pitchfork must change between the double-zero point and the N_C axis (path B_3), that is, there is a degenerate pitchfork.

With the bifurcation analysis on the simple curve, we are now in the position to classify all the dynamics near the stability boundaries. This is summarized in Figure 11. In the first quadrant, the pitchfork bifurcation is supercritical and hence paths B_1, B_2, and B_3 correspond to a smooth transition from the conductive/diffusive base state to a time-independent convective roll cell. Finite-amplitude instability prior to the bifurcation point does not exist. In the second quadrant, if the path crosses the Hopf curve as in path B_5, the base state yields stability smoothly to a time-dependent oscillatory roll cell solution. If one continues to increase the driving force, the time-dependent solution increases its period of oscillation until the heteroclinic state

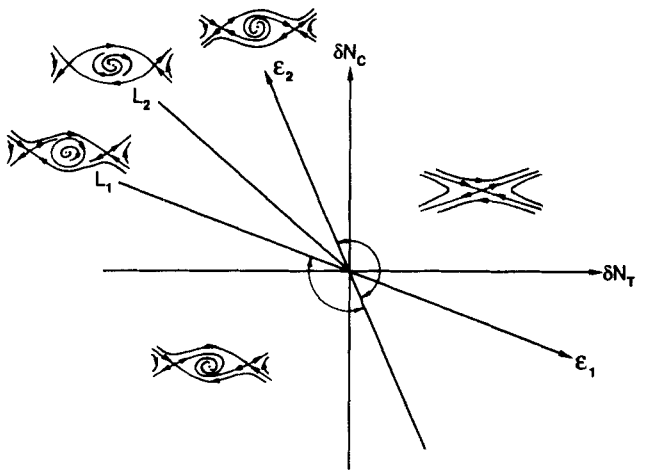

Figure 10. Dynamics near the double zero A_0 in Figure 5.
Standard parameter values: $Nu = 2$; $Sh = 10$; $Pr = 10$; $e = 0.5$
Parameters α_1 and α_2 are always positive and negative, respectively, corresponding to Figure 9a
Linear transformation of the Maragoni coordinates and unfolding parameters ϵ_1 and ϵ_2 is also evident

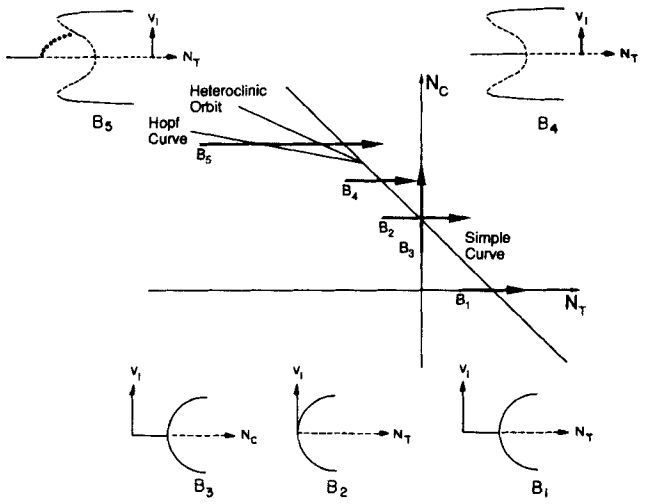

Figure 11. Bifurcation diagrams of the system in Figure 5.

Paths taken in Maragoni parameter space and corresponding bifurcation features

———, ––– Stable, unstable stationary rolls, respectively

C Oscillatory rolls

is reached. This corresponds to an infinite period of oscillation. Beyond this, the stationary rolls reappear. Most likely, one will encounter a chaotic state around that point. This has been studied numerically by Knobloch et al. (1986), who observe a period-doubling bifurcation cascade of the time-periodic roll cell solution, and a chaotic limit is reached before the heteroclinic line. We cannot resolve such global bifurcation scenarios with our present normal form analysis. It is possible to tackle it numerically, but this will not be attempted here. Right below the double-zero singularity, the phase portraits of Figure 9a indicate that the pitchfork bifurcation is subcritical, as is indicated in path B_4. In this case, the unstable roll cell solution will most likely turn around after bifurcating subcritically although we cannot resolve this with our 0(3) resolution—higher order terms would have to be computed. This implies that stable roll cell solutions exist before the critical Marangoni number and that the transition from the base state to the convective state is a

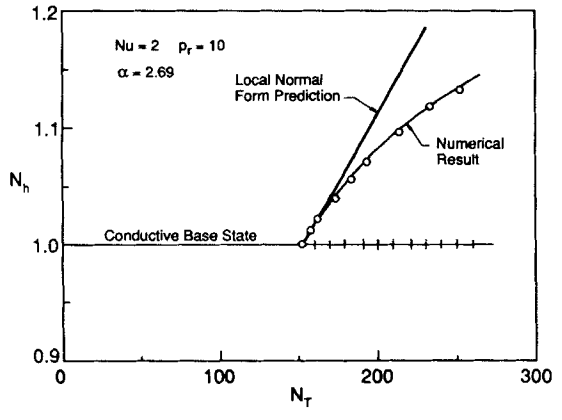

Figure 12. Enhancement of heat transfer (single gradient) predicted by local bifurcation analysis and from numerical solution of the full equations.

discontinuous one. These are unique features that should be easily identifiable experimentally. Unfortunately, detailed experiments on the Marangoni instability for the present geometry have not been carried out. Several observations have, however, been made for the closely analogous Benard problem. Platten and Chavepoyer (1972) have observed hysteresis, and Hurle and Jakeman (1969) and Shirtcliffe (1969) have seen indications of a heteroclinic bifurcation where the stationary rolls seem to replace the oscillatory rolls. These are all consistent with the dynamic portraits we depict in Figure 11.

Since path B_1 and path B_4 give rise to pitchfork bifurcations of opposite directions, it is reasonable to believe that there is a degenerate pitchfork bifurcation on the simple curve someplace between the N_C axis and the double-zero point for $e < 1$. Indeed, we detect a change in sign of ξ around this location. However, the bifurcation analysis of this higher order singularity will also await future study.

Numerical Results

We shall now focus on the enhancement of heat or mass transfer at the onset of the Marangoni instability with a single driving force. We first estimate the enhancement effect predicted by the amplitude equations of our normal form analysis. This will give the local slope of the enhancement of heat (or mass) transfer beyond the critical thermal (or solutal) Marangoni number from the normal form formulation. We then compare this local prediction with the actual enhancement obtained from the steady state solution of Eq. 20. Streamlines corresponding to fluid motion at and beyond the onset of instability are constructed to demonstrate the flow profiles of convection. We shall end our discussion by finding a correlation-like equation of the total relative Nusselt number of heat transfer Nh^* in term of Nu, Pr, and N_T.

To simplify our study, we shall consider the enhancement due to a single driving force. The efficiency of the rate of heat transfer is described by a toal effective Nusselt number Nh^* relative to the conducting base state at the bottom of the liquid film, i.e., $z = 0$. This can be evaluated simply from the following integral:

$$Nh^* - 1 = \frac{1}{d}\int_0^d \frac{\partial S}{\partial z}(z = 1)\, dx \tag{46}$$

where $d = \pi/\alpha_c$. By solving for the convective solution to amplitude Eq. 44,

$$v_1^* = \pm\sqrt{|\epsilon/\zeta|}$$

and reversing the similarity transform to obtain the corresponding u, we obtain a local expression for Nh^* for $Nu = 2$ and $Pr = 10$,

$$Nh^* = 1 + 2.177 \times 10^{-3}(N_T - N_T^c) \tag{47}$$

At N_T far away from N_T^c the normal form local prediction is no longer valid. Instead, one should solve the steady state solution of Eq. 20 for the exact enhancement. Figure 12 shows the exact enhancement obtained from the truncated ODE together with the normal form prediction. It can be seen that the normal form analysis provides excellent prediction of linear increment

at the onset of convective instability. The exact Nh^* increases linearly with δN_T at first, then it demonstrates a negative quadratic deviation as the roll cells are being established.

For a clear visualization of the roll cells created by the Marangoni instability, we construct streamlines for two different δN_T in Figure 13. The horizontal direction is scaled as a multiple of π/α_c. Note that the roll cells are established as soon as the instability starts and they expand only slightly toward the upper corners of the box as δN_T is increased. In Figure 14, the circulation rate that is the maximum stream function in the middle of the vortex, $|\psi_{max}|$, is plotted against δN_T. It is hence evident that flux enhancement is not due to growth of the vortices but rather to their circulation rates.

We shall now generalize Eq. 47 and seek an equation of the form

$$Nh^* - 1 = k\delta N_T \beta(Nu, \mathrm{Pr}) \tag{48}$$

where

$$\beta(Nu, p_r) = Nu^p Pr^q. \tag{49}$$

Note that $\delta N_T = N_T - N_T^c(Nu)$, where $N_T^c(Nu)$ is listed in Table 1. However, we shall consider δN_T as an independent variable by limiting ourselves to the neighborhood of an Nu of interest. Since the value of $k\beta(Nu,Pr)$ can be computed locally from our normal analysis, several runs with different Nu and Pr will give k, p, and q in Eq. 49. The results are summarized in Table 3. The fitted correlation, valid for $Nu \sim 1$, is

$$Nh^* = 1 + 0.001324 Nu^{0.23} Pr^{0.16}(N_T - N_T^c) \tag{50}$$

There are unfortunately few experimental data available for comparison. The closest ones are those measured by Palmer and

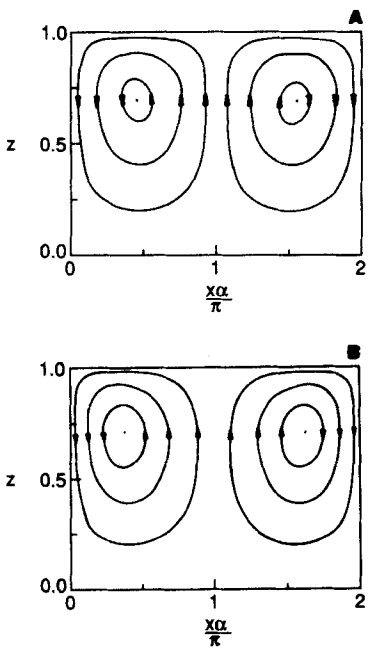

Figure 13. Numerically computed streamlines for δN_T = 10 and 100.
The size of the vortex pair is almost independent of δN_T

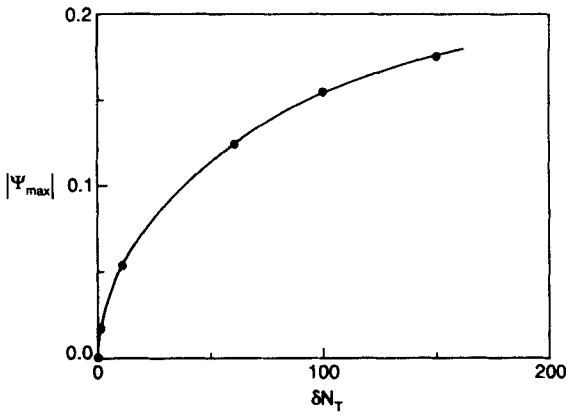

Figure 14. Circulation rate of the vortex pair as a function of δN_T.

Table 3. Second-Order Estimation of Flux Enhancement

Nu	Pr	$(Nh^* - 1)/\delta N_T$ Computed	$(Nh^* - 1)/\delta N_T$ Eq. 50	Error %
2.0	10.0	2.1720×10^{-3}	2.245×10^{-3}	3.36
1.0	3.0	1.6230×10^{-3}	1.578×10^{-3}	2.77
1.0	1.0	1.3240×10^{-3}	1.324×10^{-3}	0.00
1.0	5.0	1.7011×10^{-3}	1.729×10^{-3}	1.64
2.0	1.0	1.5328×10^{-3}	1.553×10^{-3}	1.32
2.0	5.0	2.0918×10^{-3}	2.009×10^{-3}	3.96

Berg (1971), whose geometry is exactly the one studied here, Figure 1, with the special case of a finite stagnant air phase ($Nu = k_a L/kL_a$ where k_a and L_a are the air conductivity and the air gap). Unfortunately, except for very thin liquid films (last two data points of Table 4), their measured heat transfer involves major contribution from the Benard mechanism. It is impossible to isolate this contribution from the Marangoni instability. Nevertheless, we compare in Table 4 their measured heat transfer values to the theoretical one predicted by Eq. 50. (Only the 50 and 10 cs data are listed. The 200 cs silicone oil convects almost exclusively by the Benard mechanism.) We obtain their values by measuring from their Schmidt-Milverton plots the two slopes a and c before and after the critical temperature gradient. A simple manipulation then shows the measured value is

$$(Nh^* - 1)_{\mathrm{exp}} = \left(\frac{c}{a} - 1\right) \Big/ N_T^c \tag{51}$$

Table 4. Enhancement Factor—Comparison with Experiments on Silicone Oil*

μ cs	L mm	Nu	N_T^c	$[(c/a) - 1]$	$(Nh^* - 1)_{exp}$	$(Nh^* - 1)_{theory}$
50	3.81	0.41	95.0	0.58	0.0061	0.0029
50	4.62	0.47	97.2	1.00	0.0103	0.0030
50	5.46	0.34	92.4	0.13	0.0014	0.0028
50	6.55	0.64	103.0	0.97	0.0094	0.0032
10	1.52	0.20	87.2	0.14	0.0016	0.0020
10	2.39	0.20	87.2	0.50	0.0057	0.0020

*Palmer and Berg (1971).

It can be seen from Table 4 that the experimental and theoretical numbers are of the same magnitude, with similar qualitative effects produced by Nu and Pr. Given the contribution of the Benard current, this degree of agreement is expected.

It is also instructive to compare Eq. 50 to similar studies on single-component Benard instability. There are, however, no studies with finite Nu; most results are for $Nu \rightarrow \infty$. Hence, these must be taken as upper bounds for the finite Nu cases. Schlüter et al. (1965) report an analogous expression for Benard instability,

$$Nh^* - 1 = \left(\frac{R}{R_c} - 1\right) \Big/ (0.70 - 0.00422Pr^{-1} + 0.00832Pr^{-2}) \tag{52}$$

where R is the Rayleigh number $g\beta L^3 \Delta T_o/\kappa\nu$, and R_c is the critical Rayleigh number (=1,100.6 for rigid free-boundary conditions considered here.) For $Pr > 1$, Eq. 52 is approximately

$$Nh^* - 1 \simeq 1.30 \times 10^{-3}(R - R_c) \tag{53}$$

Comparing this to values for the Marangoni instability in Tables 3 and 4, we find the coefficients to be approximately the same order. Hence, if $(R - R_c)$ and $(N_T - N_T^c)$ are of the same order, their contributions to flux enhancement are of the same magnitude. The relative magnitude of R and N_T is of course determined by the factor $\rho g\beta L^2/\sigma_T$. Thinner films will be dominated by the Marangoni mechanism. We also note that Eqs. 52 and 53 correspond to $Nu \rightarrow \infty$ (perfectly conducting gas phase) whereas the results shown in Tables 3 and 4 are for $Nu \sim 1$. Hence, as gas phase heat transfer increases—due to, say, significant turbulent convection—the Marangoni mechanism should again be dominant. Thin films with high gas phase transfer are very common in chemical industries. For example, the classic gas-side Nusselt number correlated by Gilliland and Sherwood (Sherwood et al., 1975) for mass transfer of a trace amount of liquid from its own liquid film to the gas phase in a wetted-wall column is given by

$$Sh = 0.023\left(\frac{L}{d}\right) Re^{0.83} Sc_g^{0.44} \tag{54}$$

where Re and Sc_g are the gas-phase Reynolds and Schmidt numbers relative to the stationary column, and L and d are the liquid film thickness and column diameter, respectively. Since Eq. 54 is valid for both cocurrent and countercurrent flow, it is reasonable to assume that it also applies to our case where the liquid film does not have any bulk flow. Hence, for small columns and high Re, Sh can easily reach 100. The same is also true of the Chilton-Colburn analogy for Nu in laminar and turbulent boundary layers.

Discussion and Summary

We have addressed the linear and nonlinear stability problem of a doubly-diffusive Marangoni problem. The onset of oscillatory and static rolls has been predicted. Nonlinear finite-amplitude instability and mode competition between oscillatory and static rolls have been classified near the double-zero singularity. Both phenomena occur only when the Marangoni numbers are of opposite signs. A local expression for the enhancement factor of the single-component case also has been computed and compared to available data.

We have limited ourselves to two-dimensional roll cells. In experiments, however, both hexagonal and roll cells have been observed. In fact, Pearson (1958) has pointed out that the hexagons observed in Benard's famous experiments are due to single-component Marangoni instability and not Benard instability as Benard had originally thought. It would be a considerably more difficult challenge to extend our doubly-diffusive nonlinear analysis to the hexagonal planform.

We also note that the double-zero singularity discovered here for the doubly-diffusive Marangoni number should be common to other variations of the Benard and Marangoni problems provided two driving forces are present. For example, Palmer and Berg (1972) have shown that oscillatory instability is possible for systems with both Benard and Marangoni instability. Their oscillatory stability boundary most likely emanates from a double-zero singularity. Wankat and Schowalter (1971) also uncovered a double-zero singularity for chemical-Benard instability in a liquid film. Although these double-zeros occur in physically different systems, the nonlinear dynamics in their neighborhood can only be one of the two unfoldings shown in Figure 9. Consequently, one expects the nonlinear phenomena of subcritical pitchfork bifurcation of stationary vortices and annihilation of oscillatory vortices by stationary ones in a heteroclinic bifurcation to be present in all these instabilities. The only remaining task is to relate physical parameters to the unfolding parameters ϵ_1 and ϵ_2 and to numerically construct the vortices and flux enhancement factors as we have done here for one specific example.

Acknowledgment

The present work was supported by the National Science Foundation under Grant No. ENG-8451116. The computations were carried out while the authors were at the Department of Chemical Engineering, University of Houston.

Notation

D = solute diffusivity
e = κ/D diffusivity ratio
g = gravitational constant
G = deviation concentration
h_T = heat transfer coefficient
h_m = mass transfer coefficient
k = conductivity
L = film thickness
N_C = $(\sigma_C \phi L^2/D\mu)$, concentration Marangoni number
Nh^* = dimensionless heat flux scaled with respect to conductive heat flux
N_T = $(\sigma_T \theta L^2/\kappa\mu)$, temperature Marangoni number
Nu = $(h_T L/\rho c_p \kappa)$, Nusselt number
Pr = v/κ, Prandtl number
Sh = $(h_m L/\rho D)$, Sherwood number
S = deviation temperature
x = horizontal coordinate
z = vertical coordinate

Greek letters

α = horizontal wavenumber
β = coefficient of expansion, eigenvalues
θ = base state temperature gradient
κ = thermal diffusivity
μ = viscosity
ν = kinematic viscosity
ρ = density

$\sigma_C = (\partial\sigma/\partial C)$, surface tension change with concentration (assumed constant)
$\sigma_T = (\partial\sigma/\partial T)$, surface tension change with temperature (assumed constant)
ϕ = base state concentration gradient
ψ = stream function
λ = eigenvalues

Appendix: Center Manifold Projections

At the double-zero ($\lambda = \pm i0$)

We start by writing Eq. 24 as

$$\frac{dx}{dt} = Ax + v^T U v \tag{A1}$$

and

$$\frac{dy}{dt} = By + v^T V v \tag{A2}$$

where $U = \Pi_{ijk}$, and $V = \Pi_{ilk}$; $j = 1, 2$ and $1 = 3, \ldots, I$. Note that $v^T = [x^T y^T]$. Now we approximate the center manifold by writing

$$v_j = a_j v_1^2 + b_j v_1 v_2 + c_j v_2^2 + \text{h.o.t.}, j = 3, 4, , \ldots, I \tag{A3}$$

With a simple chain rule the total derivative v_j is given by

$$\frac{dv_j}{dt} = \frac{\partial v_j}{\partial v_1}\frac{dv_1}{dt} + \frac{\partial v_j}{\partial v_2}\frac{dv_2}{dt} \tag{A4}$$

that is,

$$\frac{dv_j}{dt} = (2a_j v_1 + b_j v_2)\frac{dv_1}{dt} + (b_j v_1 + 2c_j v_2)\frac{dv_2}{dt} \qquad j = 3, \ldots, I. \tag{A5}$$

On the other hand, one writes Eq. A2 in index notation:

$$\frac{dv_j}{dt} = \Lambda_{ji} v_i + [v_1^2 \Pi_{1j1} + v_1 v_2 \cdot (\Pi_{1j2} + \Pi_{2j1}) + v_2^2 \Pi_{2j2}] + \text{h.o.t.} \tag{A6}$$

The coefficients a_j, b_j, and c_j are computed as we substitute Eq. A1 into Eq. A4 and compare coefficients of the terms v_1^2, $v_1 v_2$, and v_2^2. The results are simply

$$a_j = -(\Lambda^{-1})_{ji}\Pi_{1i1} \tag{A7}$$

$$b_j = (\Lambda^{-1})_{ji}(2a_i - \Pi_{1i2} - \Pi_{2i1}) \tag{A8}$$

$$c_j = (\Lambda^{-1})_{ji}(b_i - \Pi_{2i2}); \quad i, j = 3, 4, \ldots, I \tag{A9}$$

Now the normal form is obtained by substituting Eq. A3 into Eq. A1 and making use of the results in Eq. A7. After some algebraic manipulation, one arrives at the normal form

$$\frac{dv_1}{dt} = v_2 + A_1 v_1^3 + B_1 v_1^2 v_2 + C_1 v_1 v_2^2 + D_1 v_2^3 + 0(|v_1|^5, |v_2|^5) \tag{A10}$$

$$\frac{dv_2}{dt} = A_2 v_1^3 + B_2 v_1^2 v_2 + C_2 v_1 v_2^2 + D_2 v_2^3 + \text{h.o.t.} \tag{A11}$$

Here the coefficients are given by:

$$A_k = \sum_{i=3}^{N} a_i(\Pi_{1ki} + \Pi_{ik1}) \tag{A12}$$

$$B_k = \sum_{i=3}^{N} [a_i(\Pi_{2ki} + \Pi_{ik2}) + b_i(\Pi_{1ki} + \Pi_{ik1})] \tag{A13}$$

$$C_k = \sum_{i=3}^{N} [b_i(\Pi_{2ki} + \Pi_{ik2}) + c_i(\Pi_{1ki} + \Pi_{ik1})] \tag{A14}$$

$$D_k = \sum_{i=3}^{N} c_i(\Pi_{2ki} + \Pi_{ik2}), \; i = 1 \tag{A15}$$

This ends our center manifold computation for the normal form at the double-zero singularity point.

On the simple curve ($\lambda = 0$)

The center manifold projection method for simple bifurcation is considerably easier than that for the double-zero bifurcation. In this case, we write the system of equations as

$$\frac{dv_1}{dt} = v_i S_{i1j} v_j \tag{A16}$$

$$\frac{dv_k}{dt} = \Lambda_{0,kn} v_n + v_j S_{jk1} v_1 \tag{A17}$$

where $k, n = 2, 3, \ldots, I$ and all other summations are from 1 to I.

To approximate the center manifold we write $v_k = a_k v_1^2$ so that

$$\frac{dv_k}{dt} = 2a_k v_1 \frac{dv_1}{dt} \tag{A18}$$

Now we substitute Eq. A18 and Eq. A16 into Eq. A17 and compare coefficients for the term v_1^2. The result is $a_k = -(\Lambda^{-1})_{kj} S_{1j1}$. Finally, on applying $v_k = a_k v_1^2$ to Eq. A16, we obtain the pitchfork bifurcation form:

$$\frac{dv_1}{dt} = \epsilon v_1 + H_1 v_1^2 + H_2 v_1^3 \tag{A19}$$

where ϵ is the deviation term described in the text $H_1 = \Pi_{o,111} \cong 0$ from our numerical results, and

$$H_2 = \sum_{i=2}^{N} a_i(S_{11i} + S_{i11}) \tag{A20}$$

This completes the normal form computation for the pitchfork bifurcation on the simple curve.

Literature Cited

Berg, J. C., and A. Acrivos, "The Effect of Surface-Active Agents on Cells Induced by Surface Tension," *Chem. Eng. Sci.*, **20**, 737 (1965).

Caldwell, D. R., "Nonlinear Effects in a Rayleigh-Benard Experiment," *J. Fluid Mech.*, **42**, 161 (1970).
Carr, J., *Applications of Center Manifold Theory*, Springer-Verlag, New York, (1981).
———, "The Application of Center Manifolds to Amplitude Equations," *J. Diff. Eqs.*, **50**, 260 (1983).
Gottlieb, D., and S. A. Orszag, Numerical Analysis of Spectral Methods: Theory and Applications, SIAM, Philadelphia (1977).
Grodzka, P. G., and T. C. Bannister, "Heat Flow and Convection Demonstration Experiments Aboard Apollo 14," *Science*, **176**, 506 (1972).
Guckenheimer, J., "Multiple Bifurcation Problems of Codimension. 2," *SIAM J. Math. Anal.*, **15**(1), 1 (1984).
Guckenheimer, J., and E. Knobloch, "Nonlinear Convection in a Rotating Layer," *Geophys. Astrophys. Fluid Dynam.*, **23**, 247 (1983).
Guckenheimer, J., and D. J. Holmes, *Nonlinear Oscillations, Dynamical Systems, and Bifurcations of Vector Fields*, Springer-Verlag, New York (1983).
Ho, K. L., "Doubly-Diffusion Marangoni Instability—Enhancement of Heat and Mass Transfer by Surface-Tension Driven Connection," Master's Thesis, Univ. of Houston (1987).
Holmes, D. J., "Center Manifolds, Normal Forms, and Bifurcation of Vector Fields with Application to Coupling Between Periodic and Steady Motions," *Physica*, **2D**, 449 (1981).
Hurle, D. T. J., and E. Jakeman, "Significance of the Soret Effect in the Rayleigh-Jeffreys Problem," *Phys. Fluids*, **12**, 2704 (1969).
Hwang, S.-H., and Chang, H.-C., "Turbulent and Inertial Roll Waves in Inclined Film Flow," *Phys. Fluids*, **30**, 1259 (1987).
Knobloch, E., D. R. Moore, J. Toomre, and N. O. Weiss, "Transitions to Chaos in Two-dimensional Doubly-Diffusive Convection," *J. Fluid Mech.*, **166**, 409 (1986).
Legros, J. C., D. Rasse, and G. Thomaes, "Convection and Thermal Diffusion in a Solution Heated from Below," *Chem. Phys. Lett.*, **4**, 632 (1970).
Levich, B., "The Influence of Surface-Active Substances on the Motion of Liquids," *Phy. Chem. Hydro.*, **2**, 95 (1981).
McTaggert, C. L., "Convection Driven by Concentration and Temperature-Dependent Surface Tension," *J. Fluid Mech.*, **134**, 301 (1983).
Nagata, W., and J. W. Thomas, "Bifurcation in Doubly-Diffusive Systems," *SIAM J. Math. Anal.*, **17**, 91, 114, 289 (1986).
Palmer, H. J., and J. C. Berg, "Convective Instability in Liquid Pools Heated from Below," *J. Fluid Mech.*, **47**, 779 (1971).
———, "Hydrodynamic Stability of Surfactant Solutions Heated from Below," *J. Fluid Mech.*, **51**, 385 (1972).
Platten, J. K., and G. Chavepoyer, "Oscillations in a Water-Ethanol Liquid Heated from Below," *Phys. Lett.*, **40**, 287 (1972).
Pearson, J. R. A., "On Convection Cells Induced by Surface Tension," *J. Fluid Mech.*, **4**, 489 (1958).
Schlüter, A., D. Lortz, and F. Busse, "On the Stability of Steady Finite-Amplitude Convection," *J. Fluid Mech.*, **23**, 129 (1965).
Sherwood, T. K., R. L. Pigford, and C. R. Wilke, *Mass Transfer*, McGraw-Hill, New York (1975).
Shirtcliffe, T. G. L., "The Development of Layered Thermosultal Convection," *Int. J. Heat Mass Trans.*, **12**, 212 (1969).
Sternling, C. V. and L. E. Scriven, "Interfacial Turbulence: Hydrodynamical Instability and the Marangoni Effect," *AIChE J.*, **6**, 514 (Nov., 1959).
———, "On Cellular Convection Driven by Surface Tension Gradients," *J. Fluid Mech.*, **19**, 321 (1963).
Tavantzis, J., E. L. Reiss, and B. J. Matkowsky, "On the Smooth Transition to Convection," *SIAM J. Appl. Math.*, **34**, 322 (1978).
Villadsen, J., and M. L. Michelsen, *Solution of Differential Equation Models by Polynomial Approximation*, Prentice-Hall, Englewood Cliffs, NJ (1978).
Vidal, A., and A. Acrivos, "Nature of the Neutral State in Surface-Tension Driven Convection," *Phys. Fluids*, **9**, 615 (1966).
Wankat, P. D., and W. R. Schowalter, "Convective Stability in the Presence of a Catalytic Reaction," *AIChE J.*, **17**, 1346, 769 (1971).

Manuscript received July 27, 1987, and revision received Nov. 30, 1987.